דו"ח מדעי מסכם לתכנית מחקר מספר 20-07-0032

שנת המחקר: 3 מתוך 3 שנים

התקנים ביו-אלקטרוניים לחישה סימולטנית של פתוגנים במזון

A Bioelectronic device for simultaneous detection of foodborne pathogens

מוגש לקרן המדען הראשי במשרד החקלאות ופתוח הכפר ע"י:

ספי ורניק, המכון להנדסה חקלאית, מנהל המחקר החקלאי-מרכז וולקני

Sefi Vernick, Institute of Agricultural Engineering, ARO, The Volcani Center, HaMaccabim Rd. 68; POB 15159, Rishon LeZion 7528809, Israel

תוכן עניינים

1. תקציר מדעי

א. הצגת הבעיה

לאור התמורות הדרמטיות המאפיינות כיום את שוק המזון העולמי ושיעורי הפחת הנגרמים עקב מיקרואורגניזמים פתוגנים, נחוצים כלים דיאגנוסטיים חדשניים שיאפשר זיהוי סמנים נדיפים בספציפיות גבוהה ובזמן אמת. במחקר זה בקשנו לפתח פלטפורמה המשלבת מערך התקני טרנסיסטור תוצא-שדה (FET) המבוסס על ננו-צינורית פחמן (CNT) לחישת סמנים נדיפים של פתוגנים נפוצים במזון. עקרון החישה מבוסס על התמרה ישירה של אינטראקציה ביומולקולרית (קישור) לאות חשמלי ללא הצורך בציוד מדידה אופטי או במערכי הגבר אות. התקן כזה יאפשר ספציפיות גבוהה כיוון שהוא מכיל גלאי ביולוגי. בהשראת מנגנון ההרחה בטבע, משלב 'אף ביואלקטרוני' זה פאזה נוזלית המגבירה את רגישותו.

ב. שיטות עבודה

מתודולוגיית העבודה במחקר זה התבססה על יצירת תוצרים הנדסיים וביוכימיים, אפיונם, ושילובם לאחר מכן לכדי התקן פונקציונלי. האספקט ההנדסי כלל תכנון וייצור התקני הטרנסיסטורים (CNT-FET) ע"ג שבב (צ'יפ) תוך כדי אפיון רציף של כל שלב ע"י מיקרוסקופ אלקטרונים (SEM), מיקרוסקופ כוח אטומי (AFM), ספקטרוסקופיית RAMAN וכן, אפיון חשמלי. האספקט הביוכימי/ביוטכנולוגי כלל את תכנון ובחירת רצפי ה-DNA הקצרים המשמשים כאלמנט הכרה ביולוגית (אפטמרים), מידול יצירת המבנה השניוני שלהם, מדידת קינטיקת הקישור שלהם לסמנים הנבחרים, ופיתוח המודיפיקציה הכימית והביולוגית של ההתקן. שילוב הדיסציפלינות השונות לכדי מערכת המדידה הניסויית כלל את האפיון החשמלי של ההתקנים עם וללא אפטמרים, בנוכחות ריכוזי סמן (ליגנד) שונים.

ג. תוצאות עיקריות

לסיכום המחקר: <u>בשנת המחקר הראשונה</u> התמקדנו בבחירת האפטמרים - רצפי ה-DNA הקצרים המשמשים כגלאים (Probe) אותם נצמיד להתקן. השתמשנו במודלים ביופיזיקליים על מנת להבין את קינטיקת הקישור שלהם אל שני סמנים האופייניים לחיידקי מזון פתוגניים (הסמנים היו indole ו- Isovaleric acid, המופרשים מחיידקי E. Coli O157:H7 ו-סטפילוקוקוס S. aureus, בהתאמה). האפטמרים סונתזו עם מודיפיקציה כימית שתתאים לקישור קוולנטי ל-CNT. בצענו מידול המתבסס על NN (-Nearest neighbor), שהצביע על כך שמרבית הרצפים יוצרים באופן ספונטני מבנה שניוני בטמפ' החדר. בנוסף, בצענו headspace GC-MS למדידה עקיפה של יכולת קישור האפטמרים השונים. נוכחנו כי 26%-35% מהאינדול (כתלות בסוג אפטמר) אינו מתנדף ונותר בתמיסה, קשור לאפטמר, תוצאה המבטאת יכולת קישור באפיניות גבוהה. במקביל, נקבעו התנאים ליצירת שכבת CNT בפיזור הומוגני והדיר תוך הבנת הגורמים השונים המשפיעים על הפיזור: ריכוז, ממס ושיטת היציקה. טייבנו מתכון ליצירת שכבה צפופה של רשתות CNT כמו גם שכבה של CNT בודדות במרחקים אחידים. השכבות הנ"ל אופיינו ע"י SEM ו-AFM, שיטות המאפשרות לנו ללמוד על הפיזור והמורפולוגיה של השכבה וכמו כן, ע"י ספקטרוסקופיית RAMAN, המאפשרת לנו ללמוד על הקונפיגורציה האלקטרונית של ה-CNT. בנוסף, תכננו את ארכיטקטורת הצ'יפ. תוכננה ויוצרה מסכת

ליתוגרפיה הכוללת 12 התקני FET וכן אלק' שער. תוכננה גם המסכה לפבריקציה של תעלת המיקרו-זרימה, הנחוצה למערך המדידות. בשנת המחקר השנייה הגענו להדירות בייצור צ'יפים המכילים מערך התקני FET מבוססי רשת CNT (NTN-FET) המאפשרת ייצור סדרתי של צ'יפים בניצולת גבוהה (80% <). הצ'יפים יוצרו באופן רוטיני ב"חדר הנקי" ע"י תהליך ליתוגרפיה רב שלבי (Lift-off) בשילוב של עיבוד נוסף במעבדה (pre- and post-processing). הצ'יפים אופיינו חשמלית במערכת מדידה (probe station) ע"י מדידות זרם-מתח (I-V) המבוצעות באוויר, תוך שימוש במתח שער אחורי (backgate) או לחלופין, מתח שער אלקטרוליטי המיושם ע"י אלקטרודות השער בתעלת מיקרו-זרימה, שייצרנו במיוחד, ובה מזרימים תמיסות בופר מימיות. במקביל, מדדנו את קינטיקת הקישור של האפטמרים (בעלי "זנב" אמין, NH_2) אל הליגנדים הנבחרים באמצעות אנליזות ITC (Isothermal titration calorimetry), שיטה המאפשרת מדידה ישירה של חילוף חום ושל הפרמטריים הקינטיים (אנתלפיה, אנטרופיה ואנרגיה חופשית). למדנו שרצפים מס. 1,2, ו-4 קושרים אינדול באפיניות גבוהה ובטמפ' הקרובה (רצף מס. 1) או נמוכה משמעותית (רצפים מס. 2, ו-4) מטמפ' ההיתוך (T_m) שלהם. עקומות הקישור הראו את התרומה של אנתלפיה שלילית ושל אנטרופיה חיובית לראקציית הקישור של הרצפים 1,2 ו- 4 עם אינדול. מנגד, נוכחנו שהרצפים הללו אינם יעילים בקישור של הסמן השני, IVA, ככל הנראה כיוון שהוא פחות הידרופובי. בנוסף, יישמנו את שיטת המודיפיקציה המתוכננת ע"י סינתזה ואפיון של ריאגנט הקישור (linker). זהו ריאגנט ייחודי שאינו זמין מסחרית (פורמיל בנזן דיאזוניום) ולכן סנתזנו אותו ואפיינו אתו ע"י FTIR. חקרנו את התנאים המשפיעים על קישור ספציפי של האפטמר לננו-צינוריות הפחמן תוך שימוש בסמנים פלורסנטיים. טייבנו את תהליך המודיפיקציה (בין היתר, ע"י בחירת ה-PH , ריכוז המגיבים, טמפ' וזמן אינקובציה, פסיבציית פני שטח הסיליקון, טמפ' וזמן השטיפות), ולבסוף, הוכחנו קישור ספציפי של האפטמר אל תעלת ה-CNT. את התהליך בצענו תוך שימוש במערכת המיקרו-זרימה שייצרנו קודם לכן. בשנה השלישית למחקר, כשבידנו התקנים פונקציונליים ומאופיינים התחלנו את מדידות החישה הביו-אלקטרוניות. נוכחנו כי **לאחר חשיפה לאינדול (בריכוזים שונים) ההתקנים הביו-פונקציונליים (המותמרים באפטמרים מס. 2 ו-4) מראים תגובה חשמלית ומציגים הזזה (SHIFT) במתח ההיפוך (V_{TH}) כמו גם ירידה בזרם הנמדד, עדות ברורה לתרגום התגובה של קישור אפטמר-ליגנד לכדי אות חשמלי מדיד בטרנסיסטור.** לבסוף, על מנת לייצר התקנים מתקדמים ביותר המכילים תעלת CNT בודדת, פיתחנו תהליך איטרטיבי תוך שימוש בכלי עיבוד תמונה שאפשר לנו לנתח מאות תמונות SEM של CNT בודדות ע"ג צ'יפ ולהקיש לגבי תבנית פיזורן האופיינית. בהתבסס על תבנית זו, תכננו וייצרנו צ'יפ חדש ("דור 2") בעל מספר גבוה ביותר של התקנים פוטנציאלים. בכוונתנו לשלוח בימים הקרובים מאמר לפרסום מדעי בג'ורנל מוביל בתחום, המסכם את עבודתנו.

ד.   מסקנות והמלצות ליישום התוצאות

- פיתחנו וייצרנו התקני CNTFET ע"י טיוב תנאי שיקוע הצינוריות ע"ג הצ'יפים והתאמת ארכיטקטורת ההתקנים ותהליך הפבריקציה לתבנית הפיזור. כמו כן, ייצרנו "דור 2" של התקנים המתבסס על

3

טרנסיסטורים בעלי תעלה בודדת. בהמשך, בכוונתנו ליישם את שיטת החישה עם ההתקנים החדשים.

- איתרנו אפטמרים שלגביהם היה מידע קודם בספרות ואפיינו באופן מעמיק את קינטיקת הקישור שלהם לליגנדים הנבחרים. יש לציין כי הקינטיקה שמדדנו הייתה שונה משמעותית מזו שבספרות וכי עלה ביכולתנו לאפיין קישור באפיניות גבוהה של ליגנד אחד בלבד. בעתיד נשתמש בכלים חישוביים עדכניים לתכנון מחשב של אפטמרים. שיטה זו הינה חדשנית מאד ומייתרת את השימוש בשיטות ניסוייות "מסורתיות" כגון "SELEX".

- תהליך המודיפיקציה הכימית בוצע ואופיין, ראגנט הקישור סונתז במעבדה ואופיין, היקף הספיחה הלא-ספציפית נחקר ופותחה שיטת אקטיבציה המשפרת את יעילות המודיפיקציה ואת הספציפיות.

- קישורם הספציפי של האפטמרים (המשמשים כגלאים הביולוגיים) הוכח.

- מערך המדידה החשמלי פותח, תעלת המיקרו-זרימה יוצרה והותאמה לצ'יפ.

- מערך המדידה, הביוצ'יפים הפונקציונליים והמאופיינים (חשמלית, מיקרוסקופית) יושמו ומדידת הסמנים (מדידת מוליכות חשמלית כתלות בריכוז הסמן) בוצעה. מכיוון שלא עלה בידנו בזמן הנתון לפתח ולייצר מעגל מודפס (PCB) תפוקת המדידות שלנו הייתה איטית מהמתוכנן.

- לצערנו במהלך שתיים מתוך שלש שנות המחקר נבצר מאתנו להגיע באופן שוטף למעבדה ונגרמו עיכובים במחקר. בנוסף, תלותנו בגורמים נוספים (חדר נקי, יחידות צב"מ וכו') גם היא הוסיפה לעיכובים בלתי צפויים. בפרט, ייצור הצ'יפים נעצר כמעט לגמרי לתקופה ארוכה. אף על פי כן, עלה בידנו לעמוד במרבית יעדי המחקר וברא ובראשונה, הוכחת התכנות למדידה ביו-אלקטרונית של ליגנד (אינדול).

2. Introduction

Pathogenic microorganisms are responsible for 600 million foodborne illnesses and nearly half a million deaths annually (1). According to CDC data, about 48 million people in the U.S. are infected, 128,000 are hospitalized, and 3,000 die each year from foodborne diseases and the USDA estimates that foodborne illness costs consumers about $6.9 billion annually (2). Further upstream the agri-food chain, losses in crop yield due to pathogens are close to 40% and a similar rate is estimated in post-harvest (3, 4). Current practices are inadequate to ensure the safety and security of food during both pre-and post-harvest stages as well as processing. Using bacterial volatile organic compounds (VOCs) as biomarkers is an attractive new diagnostic approach (5) with many advantages such as noninvasiveness, ability to operate in various settings and being non-susceptible to inaccuracies due to heterogeneous distribution of pathogens in the sample (6). Rapid, accurate, sensitive, fieldable and inexpensive assays are urgently needed to identify pathogenic threats in

agricultural and food products. Therefore, a bioelectronic device is required, combining the 'E-nose' strengths such as fast response, high sensitivity, and amenability for miniaturization along with the specificity intrinsic to biological sensors.

3. Research Objectives

We seek to develop a new bioelectronic assay for the detection of pathogenic volatile biomarkers, which brings many advantages over the exiting "E-nose" technologies. Our major goal is to develop a detection method inspired by natural olfactory mechanism and to demonstrate it using a first of its kind prototype operating as a "wet nose". This new biosensing platform will be based on the integration of these building blocks: microelectronic devices, functional nanomaterials and biorecognition elements in the form of a biochip containing an array of isolated carbon nanotube-based Field-effect transistors (CNT-FETs). The array will be segmented into specific biosensing regions each aimed towards a unique volatile biomarker. Specificity is achieved by covalently functionalizing the CNT with a short DNA oligomer (aptamer) that binds a specific marker. The technology will be applied to the simultaneous detection of multiple biomarkers secreted by major prevalent foodborne pathogens. This new technology may provide a solution effective both in function and in cost, to global food safety problem.
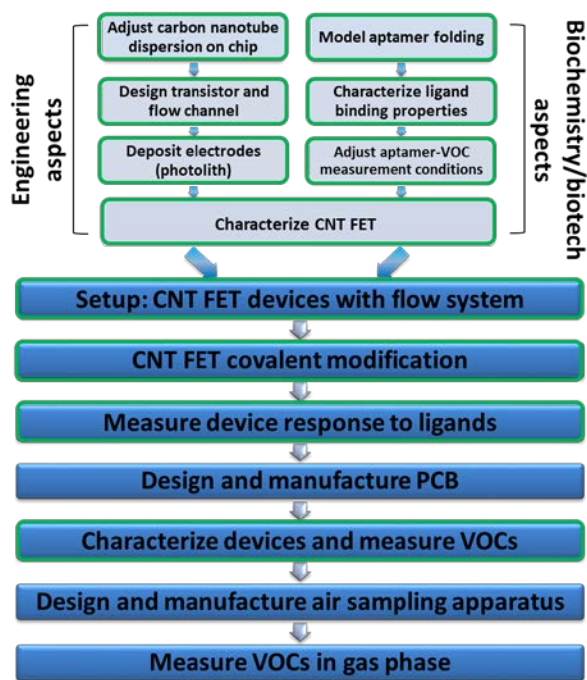

Figure 1. Experimental methodology. Tasks that were completed are circled in green.

3.1 Specific objectives and methodology .

This project consists of complementary methodologies including: Chip design and microelectronic fabrication technology, microscopic, chemical and physicochemical material characterization methods and biochemical kinetics. Briefly, during the final year our goals were to test the proposed bioelectronic ligand detection hypothesis and to pave the way towards the development of scalable bioelectronic sensor devices. Herein, we present our third and final year report. Our research methodology is schematically outlined in Figure 1.

4. Main results

Aim 1. Fabrication of CNT-FET array chip. During the 1st and 2nd years, we have invested efforts in tuning the CNT layer deposition process to reproducibly obtain a homogenous CNT dispersion on each die and in the fabrication of CNT network FET devices (CNTN-FET). Such design enables chip production at high yields and ensures a faster proof of concept. By the end of the 2nd year, we have optimized the parameters for generating a reproducible and homogenously dispersed CNT layer on a Si/SiO$_2$ chip. The layer was characterized by SEM, AFM and resonant Raman spectroscopy, as shown in Figure 2a. The preliminary design and the resulting fabricated chips are shown in Figure 2b and c. For each FET device, a CNT conducting channel was defined (as shown in Figure 2c). Titanium source and drain electrodes and platinum gate electrodes were photolithographically patterned and deposited above the CNT layer (e-beam deposition). The devices demonstrated homogenous CNT
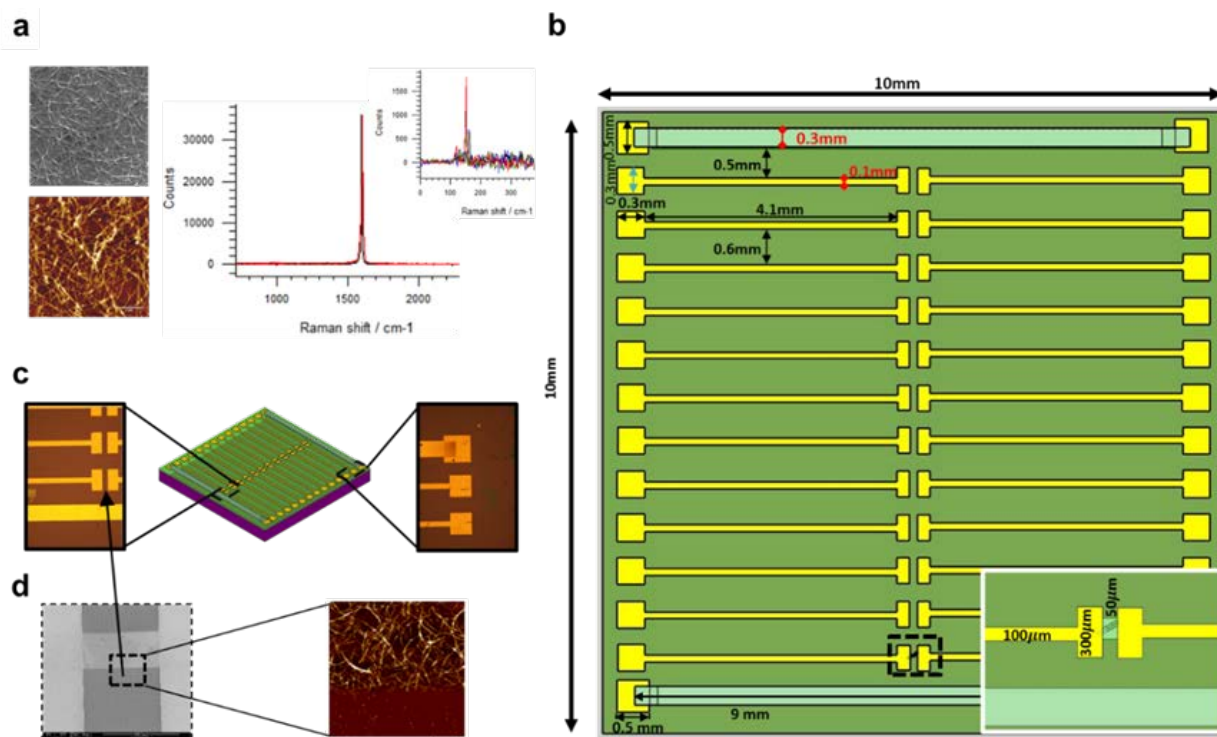

Figure 2. Fabrication of aptamer-conjugated CNT FET arrays. **a**) SEM (top left) and AFM (bottom left) images showing a homogenous CNT network dispersed on a Si/SiO$_2$ substrate. Right: raman spectra (532 nm) of two adjacent SWCNT within the layer showing the characteristic G band features ω_G^+ and ω_G^- located at 1588 cm^{-1} and 1566 cm^{-1}, respectively. Inset shows the RBM spectra of the same nanotubes, located at 170 cm^{-1} corresponding to a diameter of 1.45nm. The defect-induced D band ("Disorder mode") was not observed. **b**) A scheme of the preliminary chip design showing an array of 12 FET devices and 2 pseudo-reference (gate) electrodes. CNT networks are patterned as a FET channel of 50 µm X 100 µm (shown in inset). **c**) Platinum gate and titanium source and drain electrodes are patterned and deposited by e-beam deposition. **d**) Each CNT network device is extensively characterized structurally, using SEM and AFM, electronically by using Raman spectroscopy and finally, by measuring its I-V characteristics.

density across the chip (as shown in the SEM and AFM images of Figure 2d). Devices were further characterized structurally and electrically as previously mentioned.

Sub-aim 1.1. Optimization of SWCNT dispersion using image processing. As previously mentioned, a large number of devices are required for such a study. Therefore, a scalable spin-cast-based fabrication method, capable of placing multiple CNTs on a chip, was employed. The first goal set for the third year was to optimize the spin-cast protocol that we have developed previously and to enable a high-throughput analysis of chip-dispersed CNTs, to maximize the yield of single-crossing CNT FET devices. Consequently, it was necessary to analyze hundreds of HRSEM micrographs, which is tremendously time-consuming. We have enabled a high-throughput analysis by writing code that automates the multi-stage screening process. MATLAB image-processing tools were used to process each HRSEM micrograph, as follows: *i*) Each image was cropped and de-noised by using a Wiener filter, *ii*) Illumination equalization was applied to the images to compensate for the illumination variability commonly encountered in CCD-generated HRSEM images, *iii*) A defect correction was performed by a function that singles out observable defects on the substrate (SiO_2) surface, *iv*) Binarization of the images was performed, resulting in a white CNT on a black background image, *v*) Finally, a function that counts all CNTs was used. Figure 3 summarizes the stages in image processing.
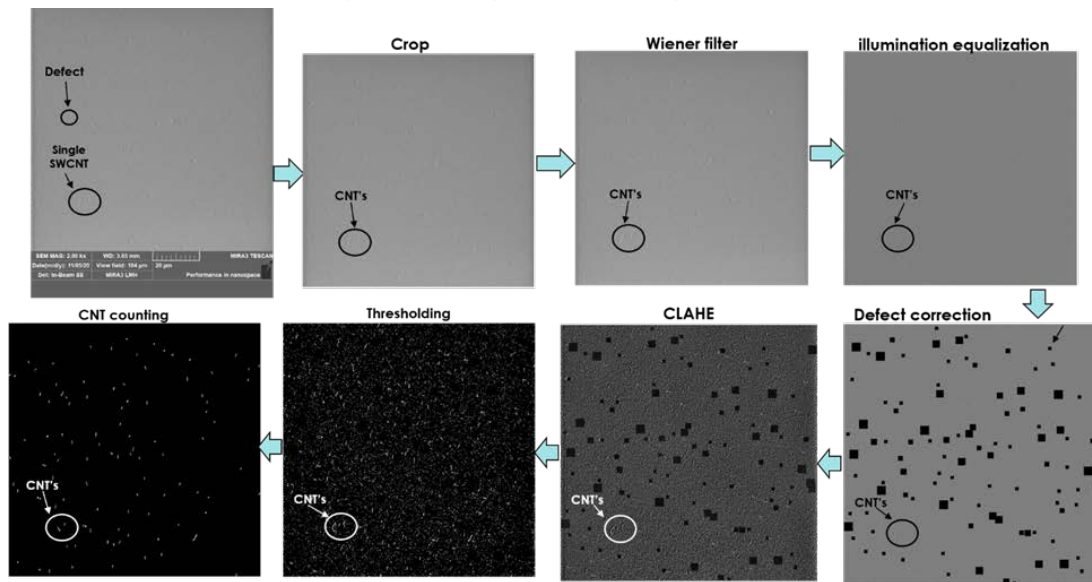

Figure 3. Image processing enables high-throughput analysis of CNT dispersion patterns. From the top left, clockwise: CNT suspensions are spun onto Si/SiO_2 chips using different conditions, and chips are scanned by HRSEM. Image processing is automated to include the following steps: first cropping the relevant areas and applying a Wiener filter. Next, illumination is equalized, and defects are marked. Finally, images are binarized such that CNTs are colored white on a black background, thus facilitating a simple automized CNT counting.

We have plotted the number and the density of CNT's *vs.* location on the chip, as depicted in Figure 4a and 4b, respectively. As an example, the mapping results of a single chip are presented.
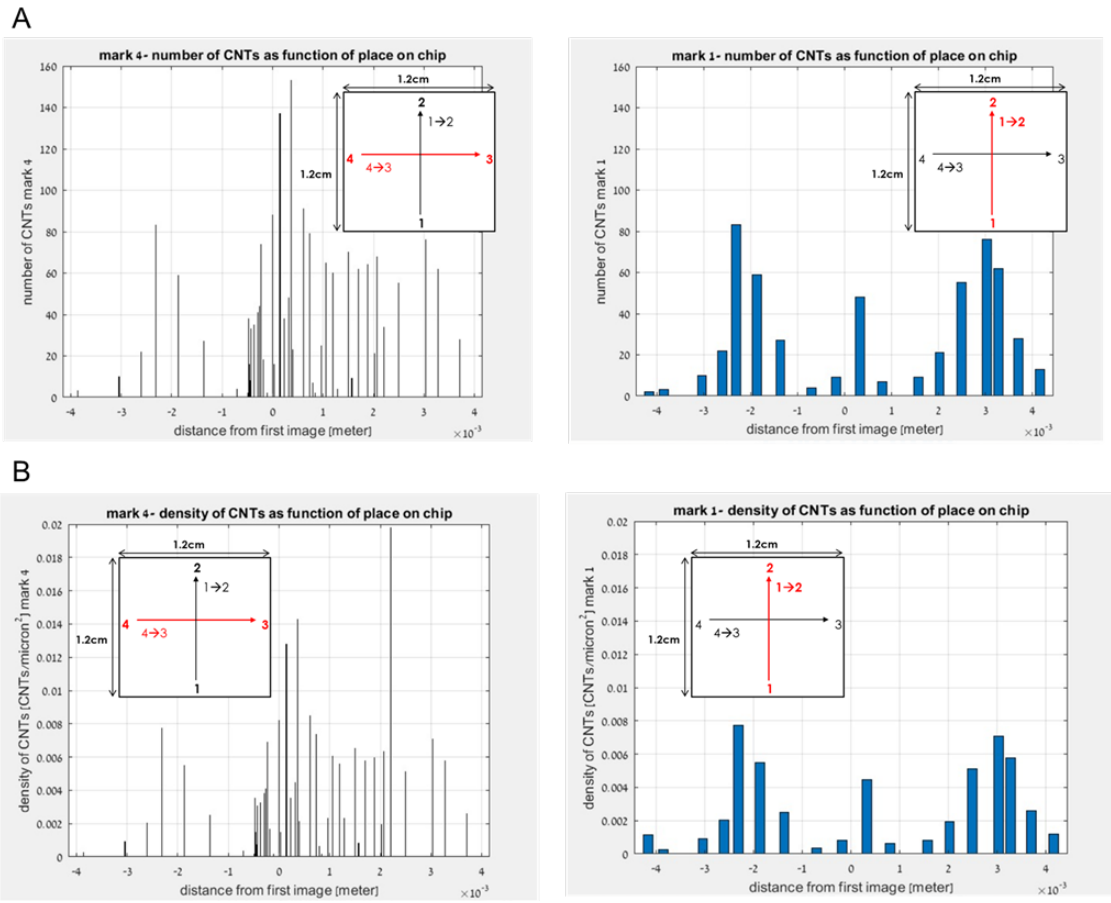

Figure 4. Number and density of dispersed CNTs on a Si/SiO$_2$ chip (1x1 cm) after spin coating. A) The number of CNTs vs. location on the chip was obtained from a horizontal scan (left) and a vertical scan (right). B) Similarly, the density of CNTs, presented as CNTs/µm^2, was plotted vs. location on the chip

The obtained results can also be presented in two-dimensional histograms, as shown in Figure 5. As indicated by the histograms, the highest CNT concentrations are found within 2-3 mm from the chip edges. This dispersion pattern is reproducible and was therefore used in the design of a second-generation FET device architecture.
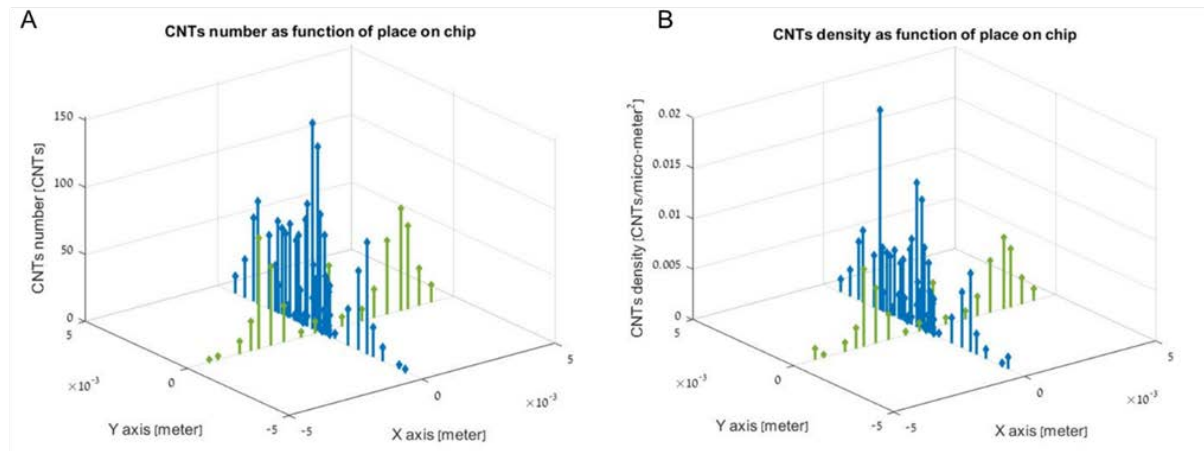
Figure 5. A two-dimensional histogram of CNT dispersion. The number (A) and density (B) of CNTs dispersed on a Si/SiO$_2$ chip (1x1 cm) were obtained from multiple SEM images.

In addition, the average length of the dispersed CNTs was found to be 1.725 ±0.1 µm, as shown in Figure 6. This parameter was helpful in determining the source-drain electrodes gap in the photolithography mask.

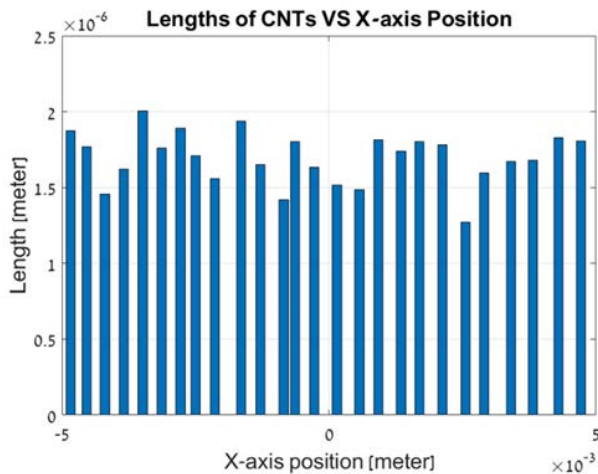**Figure 6**. Length of CNTs dispersed on a chip *vs.* location. The average length was found to be 1.725-±0.1 µm

Sub-aim 1.2. Design and fabrication of a second generation CNT-FET chip. Based on these data, we have designed a device architecture that potentially maximizes the yield of devices with single CNT crossings. Three photolithography masks were required for the devices and an additional mask for the microfluidic channel. The first mask includes all the devices, interconnects, and contact pads. As shown in Figure 7A, a total number of 92 devices were positioned in a U-shaped structure, corresponding to the dispersion pattern of the CNTs on the chip. Each device contains a round-shaped source and drain electrodes (Figure 7A, right). Such geometry is more likely to produce devices with single CNT crossings, concomitant with the random orientation of the dispersed CNTs. A circle with a diameter of *d*=50 µm comprises the source electrode that is encircled by an elliptic drain electrode with a width of 20 µm. The source-drain gap was set at 2 µm; the interconnects width = 10 µm, and the contact pads, located on two sides of the chip, were designed as

9

150 µm squares. The second mask, shown in Figure 7B, contained the on-chip gate electrodes. These pseudo-reference electrodes were designed as multiple long bars of 30-µm width, short-circuited to each other, crossing the chip in horizontal and vertical directions. The bars are contacted via contact pads on each side of the chip. A third mask, shown in Figure 7C, was designed in order to protect the CNT devices while etching all of the remaining CNTs on the chip. The mask contains 92 squares (100 µm) that are located right above the devices. Finally, an additional mask was designed to allow the fabrication of a mold for a microfluidic channel, as shown in Figure 7D. The mask comprises a U-shaped channel with a width of 400 µm positioned right above the devices. The mask also contains an inlet and an outlet with a diameter of 1 mm.
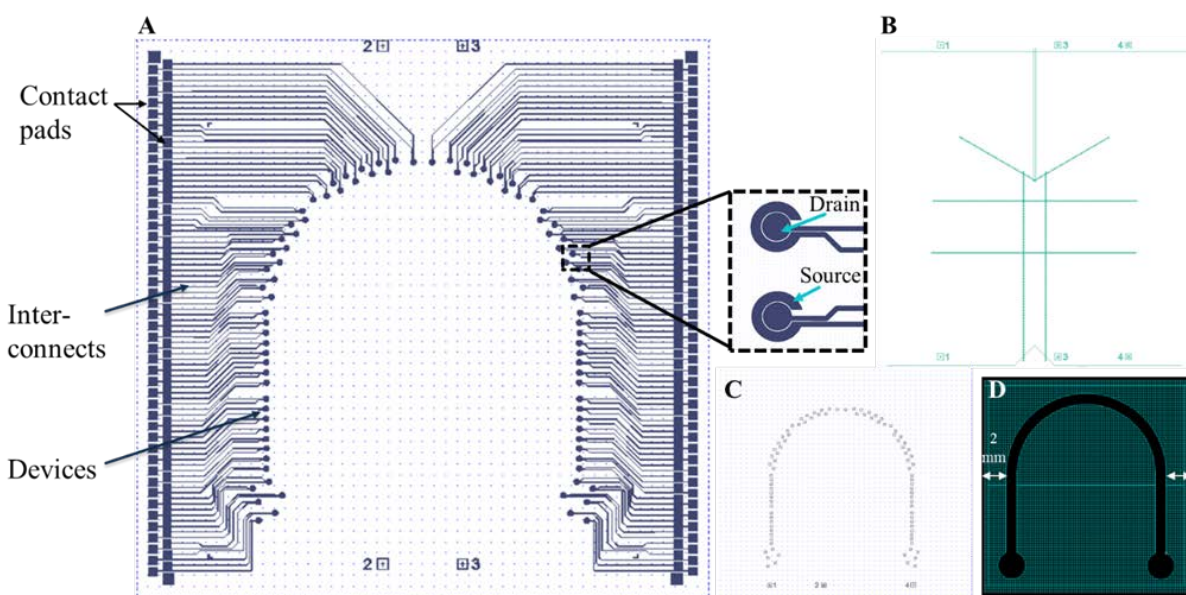

Figure 7. Design of photolithography masks. Three masks were designed (using CAD tools) based on the obtained CNT dispersion data. A) The device mask contains 92 FET devices (46 on each side of the chip) each contains source and drain electrodes contacted via interconnects to contact pads on both sides of the chip. Source-drain electrodes are designed as inner and outer circles with a gap of 2 µm. B) gate electrodes ('pseudo-reference') designed as long bars traversing the chip horizontally and vertically, and contacted via contact pads located in the chip corners C) A protection mask was designed to protect each device' CNT channels while etching all other CNTs on the chip. D) A microfluidic channel mask was designed containing a flow cell of 400 µm, with a U-shape to fit the device area. The mask also contains an inlet and outlet with a diameter of 1 mm.

The CNT-dispersed Si/SiO_2 chips were photolithographically patterned, and metal was deposited (Titanium source-drain electrodes and Platinum gate electrodes). The 'lift off' process generated individual chips, which were finally diced and characterized microscopically (Figure 8A) and by SEM (Figure 8B).
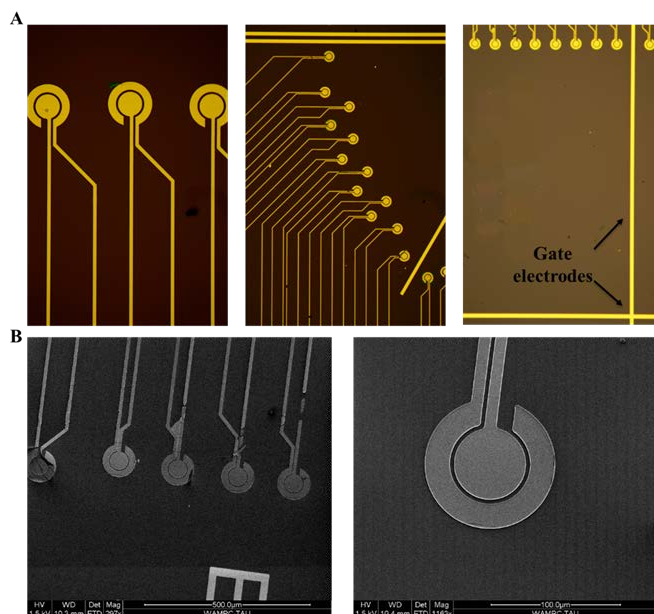
Figure 8. CNT FET chip. A) Microfabricated chips were microscopically inspected (left image at a mag. of x50, middle and right image at a mag. of x20), and, B) scanned by SEM (Bars: left image 500 µm, right image 100 µm).

Aim 2. Experimental setup. Following the complete chip fabrication and prior to measurements, devices were annealed at 400 ºC in ultra-high vacuum (Rapid thermal annealing) to reduce contact resistances and remove residual polymer from the nanotube sidewalls. Preliminary measurements were conducted by individually interrogating each device with an electronic measurement setup. These measurements include I-V and noise characteristics, and time traces (I-t). The CNT-FET chip was stamped with the PDMS microfluidic flow cell (fabricated by using the microfluidic mask, as previously described), placed directly above the devices, which includes inlets and outlets for the introduction of the electrolyte, the FBDP reagent, the aptamer, and ligands through a thin, flexible polyethylene tubing (outer diameter 1mm). A picture of the preliminary experimental setup is shown in Figure 9A. A syringe pump connected to the outlet terminal withdraws fluid exiting the channel, thus allowing full control over flow rates. An example of I-V probing of devices on a chip is shown in Fig. 9B and C transconductance plots. I-V probing was conducted in air by applying back-gate (Fig. 9B). Devices exhibited slight p-type behavior with a slope of 15 nA/V and currents ranging between 600 nA – 1.8 µA. The transfer characteristics obtained by applying an electrolytic gate (in 100 mM phosphate buffer pH 8) demonstrated ambipolar (semi-metallic) behavior, as seen in Figure 9C, fitting a model of carbon nanotube Schottky barrier transistors.
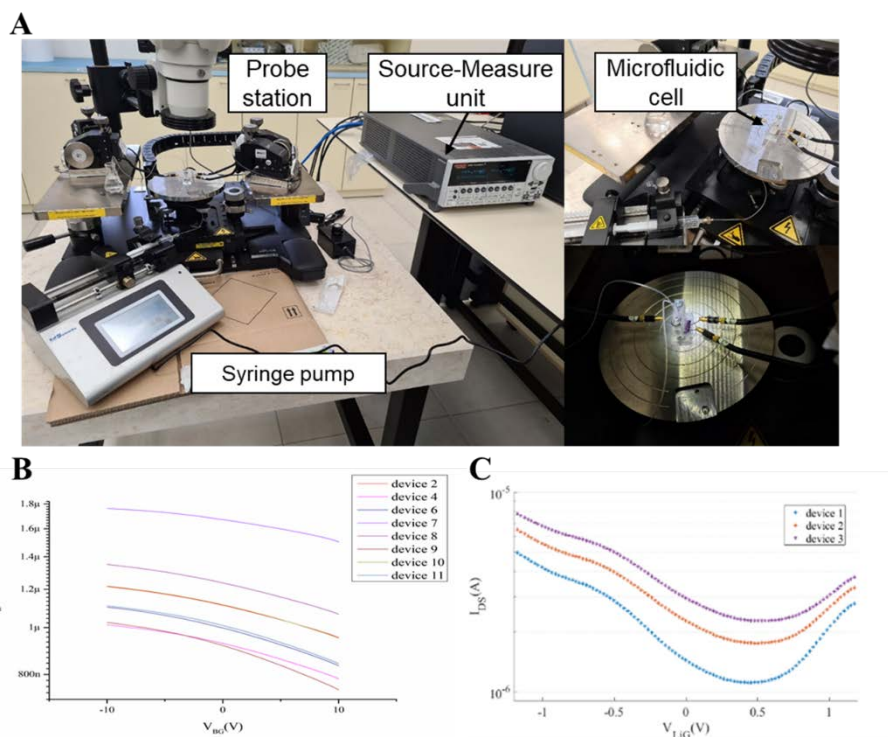
Figure 9. CNT FET experimental setup and preliminary electrical measurements. **A)** The setup includes a probe station and a source-measure unit (dual channel) that enable a thorough electric characterization of CNT-FET devices. A microfluidic flow cell is stamped on the chip (right), defining a flow channel of 400 µm wide. A syringe pump (bottom left) is used to control the flow of the introduced electrolyte and reagents. **B**) Each device is electrically characterized by measuring its I-V (transconductance) in air using the Si substrate as backgate and applying a gate bias of V_{BG}= -10V to +10V, with source-drain voltage V_{SD} = 0.1V, or, in liquid, **C)** by applying electrolytic gate (V_{LG}) via the on-chip Pt gate electrodes, V_{LG}= -1.2 V to 1.2 V and source-drain bias V_{SD} =100mV in 0.1 M potassium phosphate buffer solution pH 8. Shown here are examples of backgated and liquid gated I-V plots of four devices with semi-metallic conductance ranging between 600-1800 nA.

Aim 3. Aptamer-VOC binding interaction – kinetic study. In order to provide a proof of concept, four oligomer sequences that have demonstrated the ability to bind Indole and Isovaleric acid were selected for this study. We have synthesized the aptamer sequences with a 5' amino modifier (a custom modification consisting of an -NH2 group connected to the DNA by a short three carbon chain). The binding properties of these aptamers are associated with a formation of secondary structures, which are characterized by a melting temperature (T_m). To obtain a basic understanding of their thermodynamics we performed structural modeling using UNAfold algorithm (based on a nearest-neighbor model), as shown in **Table 1**. The model indicated that the T_m of all sequences, excluding sequence no.1, are above room temperature and that their secondary structures mostly involve stem-loop configuration, which is central to field-effect-based signal transduction. We have further studied the binding of indole to our candidate aptamers (Seq1-4) by headspace GC-MS, as shown in **Table 2**.

Our findings indicated that all aptamers are effective in binding indole: 26%-35% of the added Indole were retained in solution, bound by aptamers.
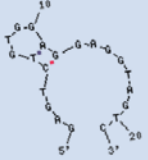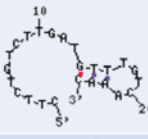
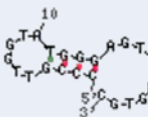Table 1. Structural modeling of the aptamers

Aptamer	Sequence	structure	ΔG (kcal.mole^{-1})	T_m (ºC)
1	5' GAG TCT GTG GAG GAG GTA GTC		0.42	17.8
2	5' CTT CTG TCT TGA TGT TTG TCA AAC		-0.72	33.4
3	5' GCG CAT TGG GTA TCT CGC CCG GCT		-1.54	44.3
4	5' CCC GTT GGT ATG GGA GTT GAG TGC		-1.35	41.6

Table 2. Headspace GC-MS analysis of aptamer-indole interaction in buffer.

	headspace indole conc.*		% Indole left in solution
	ppm	µM	
Seq 1	0.70	6.0	30
Seq 2	0.70	6.0	30
Seq 3	0.74	6.3	26
Seq 4	0.65	5.5	35

* average of three samples

Despite its advantages, HS-GC-MS analysis is performed in temperatures that are considerably higher than the corresponding melting temperatures (T_m), leading to unfolding of the aptamers and limiting the understanding of VOC-aptamer binding interactions. We have therefore used ITC (Isothermal titration calorimetry) that enables a direct measurement of the heat change upon binding and provides information about all binding parameters (affinity, stoichiometry, enthalpy and entropy) in a single experiment. We used ITC to study the interactions of seq1-4 with target ligands at 25 °C under which the aptamers are mostly folded. The experimental results and corresponding fitting curves are shown in Figure 10 and

the thermodynamic parameters obtained for the interaction of Indole with the aptamers are summarized in **table 3**.
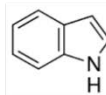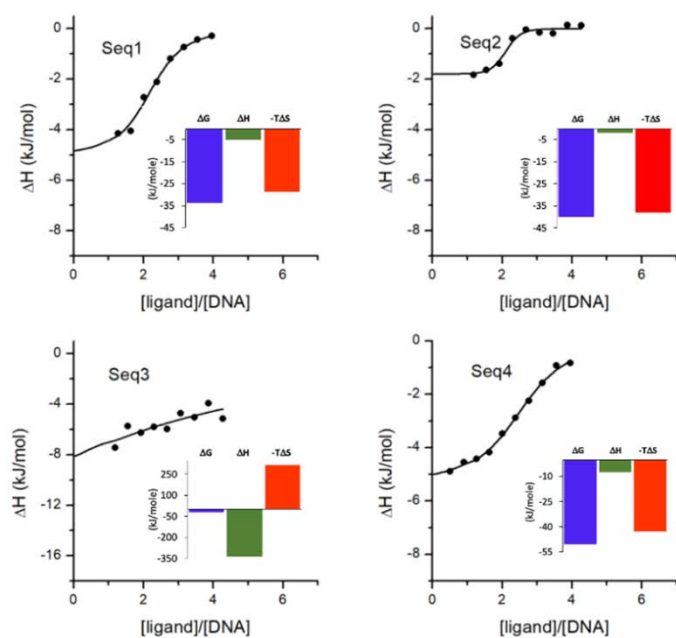
Figure 10. ITC experimental results and corresponding fitting curves for the interaction of seq1-4 with indole at 25 °C. The insets show the respective binding signature plots (free energy, binding enthalpy, and entropy factor). The sample cell contained the aptamers (12.5 μM) in solutions of 0.1 M phosphate buffer, pH 8, and 1% methanol v/v. The target ligand was dissolved in methanol and diluted to 250 μM in the phosphate buffer (achieving a final concentration of 1% methanol v/v). Injection volumes were 3.5 μl each, injection time 6 s, and delay between injections 150 s.
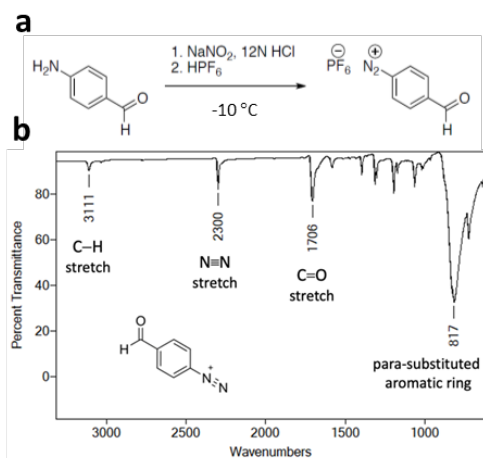
Table 3. Thermodynamic parameters for aptamer-indole interaction obtained by ITC.

	Seq1	Seq2	Seq3	Seq4
n	2.1 ± 0.1	1.92 ± 0.06	0.8 ± 3	2.6 ± 0.1
K_D (μM)	1.2 ± 0.8	0.10 ± 0.8	340 ± 1e4	2.2 ± 0.8
ΔH (kJ/mol)	-5.1 ± 0.9	-1.8 ± 0.2	-335 ± 1e5	-5.3 ± 0.6
ΔG (kJ/mol)	-33.8	-40	-19.8	-50.3
$-T\Delta S$ (kJ/mol)	-28.7	-38.1	315	-43

The results indicated that Seq1, 2 and 4 feature high binding affinities towards indole at a temperature that is very close (Seq1) or significantly lower (Seq2 and 4) to their respective T_m. Seq1 and Seq2 bind 2 Indole molecules per binding site, and Seq 3 show capability of binding 2 to 3 ligands per binding site. Fitting of Seq3 binding model with one or two sets of sites was unsuccessful. Binding signature plots (insets in figure 1) provide a detailed view of the contribution of enthalpies and entropies to the overall binding affinities and reveal additional mechanistic information. Seq1, 2 and 4 show negative binding enthalpies (characteristic of favorable hydrogen bonding). However, the main contribution to the binding affinity originates from large favorable binding entropy that is characteristic of dominant hydrophobic interactions and the accommodation of conformational changes. This observation agrees with the expected nature of interactions that should govern a molecule such as Indole, which is hydrophobic, and have little tendency to form hydrogen bonds (see structure in the upper right corner of Figure 10). In addition, induced conformational changes are expected upon entrapment of the target ligands within the binding domain. Contrary to

indole, none of the studied aptamers showed binding affinity towards IVA, which is a VOC biomarker for *Staphylococcus* (*S.aureus*). IVA is comprised of short alkyl chain and carboxylate group, prone to form hydrogen bonding and is less hydrophobic than Indole (see 2nd year report, page 8). We concluded that the selected aptamers should be more efficient for the detection of highly hydrophobic VOCs.
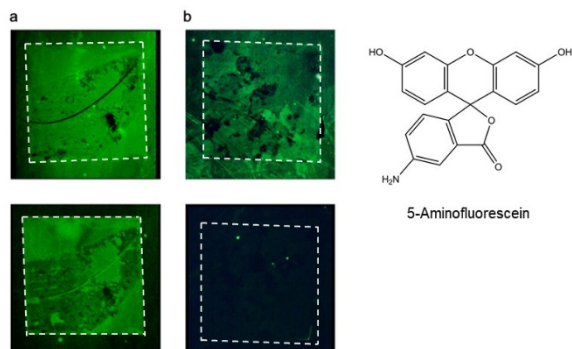
Aim 4: CNT FET covalent modification and probe attachment. Our strategy for CNT-FET functionalization was comprised of two steps: (1) CNTs modification (oxidation) by aldehyde-containing diazonium compound; (2) coupling of amine-modified aptamer to the aldehyde group via reductive amination. The diazo compound formylbenzenediazonium

hexafluorophosphate (FBDP) was synthesized as depicted in Figure 11a and characterized by FT-IR (Figure 11b). The spectrum features the IR stretch bands of the aldehyde group, the para-substituted benzene group, and the formed diazo group at 2300 cm^{-1}.

Figure 11. FBDP synthesis and characterization. **a**) Synthesis of FBDP from 4-aminobenzaldehyde. **b**) FT-IR spectrum of the synthesized FBDP.

To verify the formation of covalent attachment between FBDP and the CNTs, and to confirm our ability to couple the set of amine-modified aptamers to the aldehyde group through reductive amination, we used the fluorescent marker, 5-aminofluorescein (FITC-NH_2, upper right corner of Figure 12). Following the modification of the CNTs by FBDP, FITC-NH_2 was coupled to the CNT-FBDP layer via reductive amination. Figure 12a demonstrates the efficiency of our approach to achieve a uniform

Figure 12. Fluorescence of FITC-NH_2 at 519 nm. (**a**) Upper panel: conjugated to FBDP-modified CNTs via reductive amination immediately after fabrication. Lower panel: after 1h incubation in PBS at 60 °C; (**b**) Upper panel: adsorbed to unmodified CNTs immediately after fabrication; Lower panel: after 1h incubation in PBS at 60 °C. The dashed lines mark the boundaries of the CNTs layer.

and stable layer of FITC-NH_2, and to minimize non-specific adsorption to CNTs. The upper panel in Figure 12a shows the fluorescence response of FITC-NH_2 covalently attached to FBDP-modified CNTs. The intense response

is evident of significant FITC-NH$_2$ coverage both on the CNTs region (marked by dashed lines) and on the bare SiO$_2$ margins. The lower panel in Figure 12a shows the same sample after 1h incubation in PBS at 60 °C. Markedly, intense fluorescence could be observed solely within the CNTs region even after prolonged incubation at an elevated temperature. By contrast, incubation under the same conditions of non-specifically adsorbed FITC-NH$_2$ layer (upper panel in Figure 12b) resulted in its complete removal, as evident by the lack of fluorescence signal (lower panel in Figure 12b).

Sub-aim 4.1: Receptor attachment with flow system. We proceeded to establish conditions for receptor attachment with the microfluidics setup. Sequential modification of the CNTs with FBDP and receptor coupling via reductive amination were performed by flowing the reagents through 200 (w) x280 (h) µm^2 channel that confines the entire CNTs region and partial areas of the Ti electrodes (as shown in Figure 13, left). The covalent attachment of FITC-NH$_2$ to the CNTs is evident. Adsorption to the bare SiO$_2$ is also visible, as shown in Figure 13.
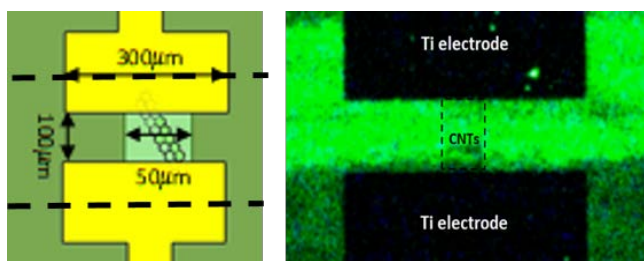

Figure 13. Fluorescence response of FITC-NH$_2$ coupled to FBDP-modified CNT FET. The attachment performed with flow system where reagents applied to confined region of 200 (w) x280 (h) µm^2 (marked by dashed lines in the left scheme. The scheme is not in scale).

In order to achieve selective attachment without the necessity of rigorous washing and sample heating, we have passivated the SiO$_2$ surface with propyltrimethoxysilane (TMPS). In addition to creating a physical barrier, formation of hydrophobic surface by the propyl residue is expected to repel incoming polar and/or charged molecules such as aptamers. Figure 14 demonstrates the implementation of our approach for attaching seq1 aptamer labeled with Cy3 fluorophore to CNT FET devices. Figure 14a shows a device that was
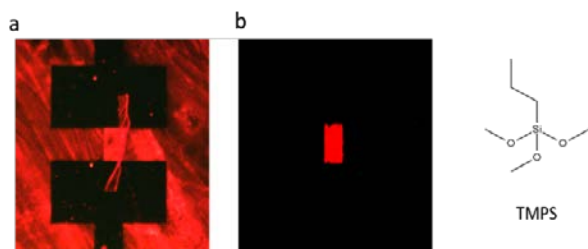
Figure 14. Selective attachment of Cy3-labled seq1 aptamer to CNT FET. (**a**) CNT FET device without TMPS (**b**) CNT FET device pretreated with TMPS. The samples were incubated in solution of 0.1 µM aptamer for 90 min at 4 C and then in PBS for 15 min at 60 C. Fluorescence emission was collected at 570 nm.

incubated in aptamer solution without TMPS activation, and Figure 14b shows a similar device that was treated with TMPS prior to incubation with the aptamer. While prominent

amount of aptamer was adsorbed to the bare SiO_2 surface (not treated with TMPS), the TMPS treated device shows selective adsorption to CNTs.

Aim 5. Bioelectronic measurement of ligands. In our final task we have studied the response of the aptamer-functionalized CNT FET device to our model pathogen marker, indole. Following covalent functionalization, CNT FET devices are expected to demonstrate higher resistivity due to introduction of defects (sp^3 defects) on the CNT lattice. In fact, the addition of a single sp^3 defect has been shown to reduce transconductance from $h/4e^2$ to $h/2e^2$ (h is Planck's constant and e the electron charge) [7, 8]. In our case, the generation of multiple defects on a CNT network channel has dramatically affected its transfer characteristics, transforming a nearly metallic CNT channel to an ambi-polar (semi-metallic) conductance, as shown in Figure 15 for a CNT FET device before and after FBDP modification. Reaction of diazonium with a sp^2-hybridized carbon atom on the surface of the SWCNT results in a covalent bond and re-hybridization of the SWCNT surface carbon atom to sp^3 [9, 10], reducing the conductance. Before and after functionalization, the current noise spectrum is dominated by 1/f noise (flicker noise). Following diazonium modification, the defect site dominates charge-carrier scattering rendering the rest of the SWCNT surface less sensitive to charge traps [11, 12]. Several mechanisms are known to be responsible for biosensing in CNT transistors with the dominant ones being electrostatic gating and Schottky barrier effect. I-V_{lg} transfer curves are instrumental in defining these mechanisms [13, 14]. Adsorbed charged species that induce a screening charge (doping) in the SWNT shift the I-V_{lg} curve along the voltage axis [15]. In addition, a decrease in in the absolute value of I_{DS} is related to a drop of the mobility μ of the carriers because of the surface scattering induced by the presence of the charged analyte in proximity of the CNT channel [16]. As seen in Figure 15, the covalent immobilization of the negatively charged DNA aptamer resulted in a decrease in I_{DS}, as expected. Following introduction to indole (20µM of indole incubated for 10 min), I_{DS} was significantly decreased and the threshold voltage, V_{TH}, demonstrated a negative shift.
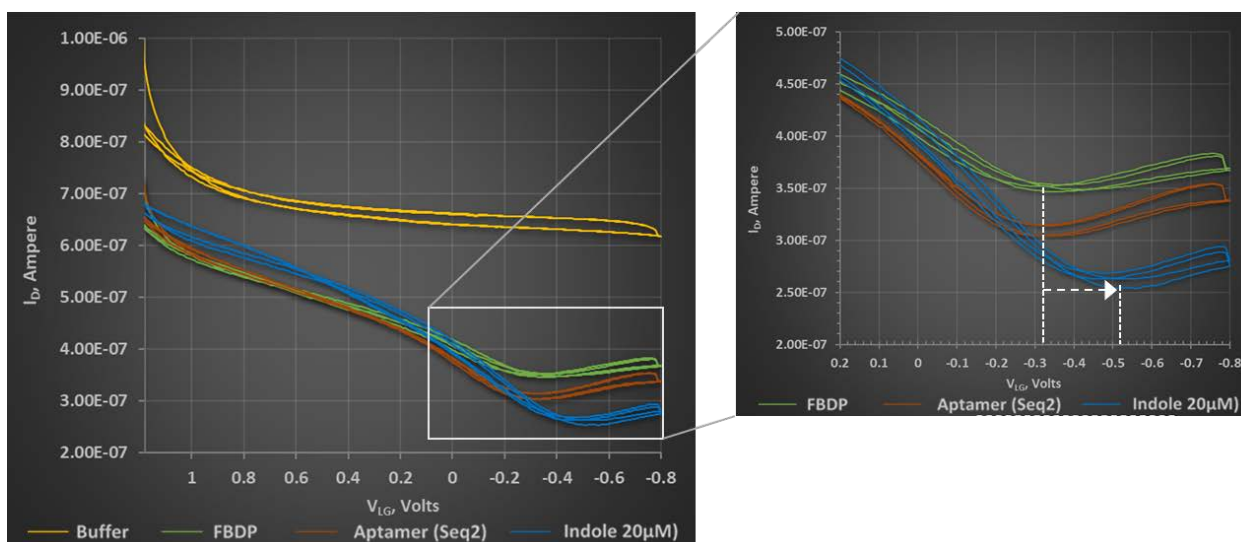
Figure 15. Bioelectronic detection of indole. An example for the electronic response of a CNT FET device following modification, aptamer conjugation, and exposure to ligand are shown (left). A pristine device demonstrates a metallic behavior that dramatically changes following FBDP modification (green curve). Further functionalization with aptamer affects a decrease in the device conductance. Following exposure to the indole (20 µM) the device demonstrates a further decrease in conductance as well as a local electrolytic gating effect (marked by dashed white lines in the zoomed-in area shown right).

In aptamer complexes, the basis for the specific recognition of a ligand lies in the enclosure of large parts of the ligand by the nucleic acid, which provides numerous discriminatory intermolecular contacts. Ligand binding pockets are formed through the formation of a number of canonical and non-canonical long-range base pairing interactions and base triples [17]. The dynamics of ligand binder systems can be broadly described by conformational selection or induced fit. Induced fit in aptamer complexes has been previously studied using aptamer models exhibiting stem-loop conformation. Structural stabilization upon ligand binding often times leads to different base-pairing patterns as the nucleic acid folds into a form with a well-defined binding pocket [18]. Evidence for the induced-fit mechanism of aptamer binding were provided by many structural and thermodynamic studies using the ATP-binding aptamer [19], the L-argininamide binding aptamer [20], the thrombin-binding aptamer [21], and the cocaine binding aptamer [22]. Our results are consistent with the stabilization of the secondary structure upon ligand binding. Following the introduction of Indole, the multiple aptamer complexes, which are immobilized to the CNT network channel, assume stable conformations. These conformers directly affect the mobility of charge carriers within the CNT channel since they cause re-distribution of charge densities, thus affecting an electric field in close proximity to the CNT lattice.

5. Summary

In this study, we aimed at implementing a new bioelectronic sensing approach that is based on direct electronic, real-time, label-free detection through nanoscale field-effect transistors. Our main goal was to develop a platform assay that comprises CNT-based FET devices, fabricated on a Silicon chip, covalently functionalizing them with indole-binding DNA aptamers, and demonstrate the feasibility of electronic detection of indole, a hallmark biomarker of the foodborne pathogen, *E. coli O157:H7*. Our objectives spanned various disciplines, as depicted by the research methodology presented in Figure **1.**

Several biochemistry/biotechnology related objectives were set for this research, most of which were accomplished during the first 24 months. Biorecognition elements in the form of short DNA aptamers were identified and custom-synthesized. Preliminary indication for the aptamer' s binding affinity to Indole was obtained by modeling and experimentally, by headspace GC-MS study. A further in-depth kinetic study, by using ITC, revealed relatively high binding affinities towards indole governed by large binding entropies. This kinetics suggested that binding-induced secondary structures likely involve large conformational changes, which may contribute to an electric field effect.

The electrical engineering and molecular electronics aspects were fully addressed during 36 months of research. CNT-FET device fabrication flow was developed and optimized. Fabrication process, including photolithography, and pre- and post-processing was standardized and routinely carried out. Chips containing CNT FET arrays were also characterized microscopically (SEM, AFM), electrically (I-V probing) and spectroscopically (Raman). During the last year, we have also aimed at scaling up our device yields by developing a process for single CNT FET devices instead of CNT network devices. Integration of the different research aspects occurred mostly during the second year. A chemical modification process was developed by synthesizing a diazonium reagent (FBDP) and demonstrating its effectiveness and specificity in coupling to CNT devices. Furthermore, we have demonstrated our ability to functionalize CNTs with DNA probes (aptamers). Aptamers were shown to specifically bind to CNT-FETs while non-specific adsorption was nearly eliminated following surface activation. In addition, an experimental setup was developed including a microfluidic flow cell and measurement setup.

Finally, we have measured the response of aptamer-functionalized CNT FET devices to different concentrations of indole. We have provided preliminary evidence to bioelectronic

sensing of indole demonstrated by altered trans-conductance curves. The generation of defects on the CNT channel lattice rendered it sensitive to charge, clearly visible by the shift in threshold voltage and impaired mobility following aptamer functionalization. Binding of indole affects conformational change that is sufficiently stable and was manifested by a further decrease in device conductance.

It should be noted that several objectives, particularly these concerning the engineering aspects of the research, were not accomplished. Notably, the design and manufacture of a printed circuit board (PCB) that was supposed to significantly increase measurement throughput; The adjustment of the setup to enable air-sampling; and, providing a proof-of-concept for bioelectronic detection using a model of contaminated food samples (spiked with bacterial pathogens).

Within this context, it should be mentioned, that during the COVID pandemic of 2020-2021 our research capacity was dramatically reduced. In particular, work was hampered by the absence of workforce, lack of critical resources such as materials and reagents due to hindered supply chains, and above all, fabrication facilities were unavailable for long periods of time affecting our chip pipeline. Nevertheless, we would like to emphasize that **the most important goal of this research – a feasibility demonstration of indole bioelectronic detection by a novel CNT-FET device, was achieved**.

References

1   WHO. *Global burden of foodborne diseases*, <http://www.who.int/foodsafety/areas_work/foodborne-diseases/ferg/en.(2015) </

2   USDA. (2020). "Foodborne Illness: What Consumers Need to Know." from https://www.fsis.usda.gov/wps/portal/fsis/topics/food-safety-education/get-answers/food-safety-fact-sheets/foodborne-illness-and-disease/foodborne-illness-what-consumers-need-to-know.

3   Savary, S., A. Ficke, J. N. Aubertot and C. Hollier (2012). "Crop losses due to diseases and their implications for global food production losses and food security." Food Security **4**(4): 519-537.

4   Fang, Y. and R. P. Ramasamy (2015). "Current and Prospective Methods for Plant Disease Detection." Biosensors-Basel **5**(3): 537-561

5   Fleming-Jones, M. E. & Smith, R. E. Volatile organic compounds in foods: A five year study. *J Agr Food Chem* **51**, 8120-8127, doi:10/1021.jf0303159.(2003)

6   Senecal, A. G., Magnone, J., Yeomans, W. & Powers, E. M. in *Environmental and Industrial Sensing.* 11 (SPIE.

7   Wilson, H.; Ripp, S.; Prisbrey, L.; Brown, M. A.; Sharf, T.; Myles, D. J. T.; Blank, K. G.; Minot, E. D. *The Journal of Physical Chemistry C* 2016, 120, (3), 1971-1976.

8   Lee, Y.-S.; Nardelli, M. B.; Marzari, N. *Phys Rev Lett* 2005, 95, (7), 076804.

9   Bahr, J. L. et al. Functionalization of carbon nanotubes by electrochemical reduction of aryl diazonium salts: a bucky paper electrode. J. Am. Chem. Soc. 123, 6536–6542 (2001).

10 Schmidt, G., Gallon, S., Esnouf, S., Bourgoin, J. P. & Chenevier, P. Mechanism of the coupling of diazonium to single-walled carbon nanotubes and its consequences. Chemestry 15, 2101–2110 (2009).

11 Vernick, S.; Trocchia, S. M.; Warren, S. B.; Young, E. F.; Bouilly, D.; Gonzalez, R. L.; Nuckolls, C.; Shepard, K. L. Nature Communications 2017, 8, 15450

12 Lee, Y.; Trocchia, S. M.; Warren, S. B.; Young, E. F.; Vernick, S.; Shepard, K. L. *Acs Nano* **2018**

13 Shkodra et al Appl. Phys. Rev. **8**, 041325 (2021)

14 Heller I, Janssens AM, Männik J, Minot ED, Lemay SG, Dekker C. Identifying the mechanism of biosensing with carbon nanotube transistors. Nano Lett. 2008 Feb;8(2):591-5.

15 Chen, R. J.; Choi, H. C.; Bangsaruntip, S.; Yenilmez, E.; Tang, X.; Wang, Q.; Chang, Y. L.; Dai, H. J. Am. Chem. Soc. 2004, 126, 15631568

16 B. L. Allen, P. D. Kichambare, and A. Star, "Carbon nanotube field-effecttransistor-based biosensors," Adv. Mater. 19, 1439–1451 (2007).

17 Noeske, J.; Buck, J.; Fürtig, B.; Nasiri, H. R.; Schwalbe, H.; Wöhnert, J. Interplay of "induced Fit" and Preorganization in the Ligand Induced Folding of the Aptamer Domain of the Guanine Binding Riboswitch. *Nucleic Acids Res.* **2007**, *35* (2), 572–583.

18 Bishop, G. R.; Ren, J.; Polander, B. C.; Jeanfreau, B. D.; Trent, J. O.; Chaires, J. B. Energetic Basis of Molecular Recognition in a DNA Aptamer. *Biophys Chem* **2007**, *126* (1–3), 165–175

19 Munzar, J. D.; Ng, A.; Juncker, D. Comprehensive Profiling of the Ligand Binding Landscapes of Duplexed Aptamer Families Reveals Widespread Induced Fit. *Nat. Commun.* **2018**, *9* (1), 343

20 Wood, A. E.; Bishop, G. R. Probing the Structure of DNA Aptamers with a Classic Heterocycle.*Molecules* **2004**, *9* (3), 67–85

21 Arnaut, V.; Langecker, M.; Simmel, F. C. Nanopore Force Spectroscopy of Aptamer-Ligand Complexes. *Biophys J* **2013**, *105* (5), 1199–1207.

22 Shoara, A. A.; Churcher, Z. R.; Steele, T. W. J.; Johnson, P. E. Analysis of the Role Played by Ligand- Induced Folding of the Cocaine-Binding Aptamer in the Photochrome Aptamer Switch Assay. *Talanta* **2020**, *217*, 121022